Arabian Journal of Chemistry (2023) **16**, 104452

King Saud University

Arabian Journal of Chemistry

www.ksu.edu.sa
www.sciencedirect.com

ORIGINAL ARTICLE

Promotional effect of nitrogen-doped and pore structure for the direct synthesis of hydrogen peroxide from hydrogen and oxygen by Pd/C catalyst at ambient pressure

Donghai Jiang [a,b,c,d], **Yongyong Shi** [a,c], **Liming Zhou** [a,c,d], **Jun Ma** [a,c], **Hongyan Pan** [a,c,*], **Qian Lin** [a,c,*]

[a] *School of Chemistry and Chemical Engineering, Guizhou University, Guiyang, Guizhou 550025, China*
[b] *State Key Laboratory of Public Big Data, Guizhou University, Guiyang, Guizhou 550025, China*
[c] *Guizhou Key Laboratory of Green Chemical and Clean Energy Technology, Guiyang, Guizhou 550025, China*
[d] *School of Chemical Engineering, Guizhou Institute of Technology, Guiyang, Guizhou 550003, China*

Received 1 September 2022; accepted 20 November 2022
Available online 24 November 2022

KEYWORDS

Pd catalyst;
H_2O_2 directly synthesizing;
Porous carbon;
Nitrogen-doped;
DFT

Abstract Nitrogen-doped porous carbon is potential support for directly synthesizing H_2O_2 from H_2 and O_2. Here, density functional theory (DFT) was used to study the effect of *N*-doped porous carbon on H_2O_2 directly synthesized. The theoretical calculation results showed that *N*-doped improved H_2O_2 productivity and H_2 conversion by increasing the dispersion of Pd nanoparticles and the Pd^0/Pd^{2+} ratio. However, *N*-doped decreased H_2O_2 selectivity by reducing oxygen's dissociation energies. The experimental results showed that adjusting the pore structure of *N*-doped porous carbon could improve the adverse effects of *N*-doping for H_2O_2 selectivity. The H_2O_2 productivity and selectivity of Pd/C catalyst with a macropore-mesoporous-microporous hierarchical porous structure were up to 328.4 $mol_{H2O2}{\cdot}kg_{cat}^{-1}{\cdot}h^{-1}$ and 71.9 %, respectively, at ambient pressure. The macropore structure enhances the transfer and diffusion performance of the catalyst and effectively inhibits the effect of *N*-doping on O—O bond dissociation, which improves H_2O_2 productivity and selectivity. This research provides a possible solution for designing a high-performance Pd/C catalyst to directly synthesize H_2O_2 from H_2 and O_2 at ambient pressure.

* Corresponding authors.
E-mail addresses: hypan@gzu.edu.cn (H. Pan), linq@gzu.edu.cn (Q. Lin).
Peer review under responsibility of King Saud University.

Production and hosting by Elsevier

https://doi.org/10.1016/j.arabjc.2022.104452

1. Introduction

Hydrogen peroxide (H_2O_2), as a green and environment-friendly oxidant, is widely used in chemical, biological, environmental, and other industries. Currently, H_2O_2 production is mainly based on the anthraquinone autoxidation (AO) process. However, the AO process has complicated processes, high production costs, and an unfriendly environment, and the safety risks of high-concentration hydrogen peroxide during transportation, storage, and use cannot be ignored (Fukuzumi et al., 2021). The direct synthesis of H_2O_2 from H_2 and O_2 has broad application prospects because of its environmental-friendly, economic efficiency, ready-to-use, and only water as a by-product (Huynh et al., 2021; Lewis and Hutchings, 2018).

Although H_2O_2 directly synthesizing has excellent potential, the formation of H_2O_2 and H_2O from H_2 and O_2, the hydrogenation and decomposition of H_2O_2 are both thermodynamically favorable (Han et al., 2021), which makes the preparation of high-performance hydrogen peroxide catalysts more difficult. Many experimental and theoretical studies (Han et al., 2021; Agarwal et al., 2021; Tian et al., 2017; Hang and Chung, 2020; Lari et al., 2017; Lyu et al., 2019; Priyadarshini et al., 2021) were conducted to obtain high-performance hydrogen peroxide catalysts. Palladium is the practical active catalyst for H_2O_2 directly synthesizing. The Langmuir-Hinshelwood reaction mechanism and proton-electron transfer reaction mechanism are the two main reaction mechanisms for directly synthesizing hydrogen peroxide (Han et al., 2021). These two mechanisms agree for oxygen adsorption but diverge for hydrogen adsorption and dissociation. According to the Langmuir-Hinshelwood reaction mechanism, hydrogen is dissociated on the surface of Pd to form H* (* indicates adsorption on the catalyst surface), and then H* and O_2* to form –OOH* intermediate. In comparison, the proton-electron transfer reaction mechanism involves hydrogen dissociated on the surface of Pd to form protic hydrogen (H^+) and electrons. Electrons are transferred to O_2* by the catalyst, and then the proton H^+ reacts with O_2* to form –OOH* intermediate. The DFT study concluded that both reaction mechanisms are inverse thermodynamically feasible (Agarwal et al., 2021). Although the mechanism of hydrogen peroxide generation is still somewhat controversial, the role of palladium as an active catalytic center is recognized; therefore, the modulation of palladium can directly affect the synthesis of hydrogen peroxide and ultimately obtain a high-performance catalyst. Changing the catalyst's synthesis process and heat treatment conditions could change palladium's geometry and electronic structure (such as particle size, crystal plane, and Pd^0/Pd^{2+} ratio), which are conducive to improving H_2O_2 selectivity and production rates (Tian et al., 2017; Hang and Chung, 2020; Lari et al., 2017; Lyu et al., 2019; Priyadarshini et al., 2021; Han et al., 2017). Alloying Pd with various metals (e.g., Au, Ag, Zn, Sn, Co, Ni) (Li et al., 2018; Ricciardulli et al., 2021; Doronkin et al., 2020; Gu et al., 2016; Wilson et al., 2018; Wilson et al., 2018; Kanungo et al., 2019; Nazeri et al., 2021; Tian et al., 2017; Kazici et al., 2017; Zhang et al., 2021; Lee and Chung, 2020; Maity and Eswaramoorthy, 2016; Zhang et al., 2018) enhance H_2O_2 selectivity by changing the geometric and electronic structure of palladium.

Support modification is another important strategy to improve the catalytic performance of Pd catalysts. The surface properties of the support can adjust H_2O_2 productivity and H_2O_2 selectivity by affecting the morphology, dispersion, electronic state and alloying degree of the Pd active metal. Support regulation of oxide (SiO_2, Al_2O_3, TiO_2, etc.) and carbon materials (Lewis and Hutchings, 2018; Vu et al., 2021; Liang et al., 2020; Edwards et al., 2014; Edwards et al., 2009; Piccinini et al., 2012; Villa et al., 2016; Hu et al., 2014; Gudarzi et al., 2015; Gudarzi et al., 2015; Thuy Vu et al., 607 (2020).; García et al., 2015) (activated carbon, ordered mesoporous carbon, CNT, etc.) are common in H_2O_2 directly synthesizing. Hutchings (Edwards et al., 2009; Ntainjua et al., 2008) and co-workers found that porous carbon supports were the best supports for Pd and Au-Pd catalysts because of the superior catalytic activity and lowest rate of H_2O_2 hydrogenation and decomposition side reactions. In the follow-up research works, the team further found that nitric acid pretreatment of carbon supports for Au-Pd catalysts could switch off the sequential H_2O_2 hydrogenation and decomposition side reactions compared with TiO_2, ZrO_2, CeO_2 and other oxide supports, making porous carbon become a significant support for the direct synthesis of H_2O_2 from H_2 and O_2.

N-doped is an effective modification method for porous carbon, which could change the surface properties and pore structure and provide plentiful chemically active sites (Wei et al., 2018). Perathoner (Abate et al., 2010) and co-workers found that the Pd-based catalysts supported on *N*-doped CNTs showed higher catalytic activity and turnover, and the improvement of this activity may be related to the electronic effect of N sites in the support. Rosa Arrigo (Arrigo et al., 2014; Arrigo et al., 2016) and co-workers believed that the N functional groups on the surface of carbon support could form a robust Pd-N bond with Pd, which could not only inhibit the agglomeration of Pd nanoparticles but also provide electrons to Pd, thus improving the stability and activity of Pd catalyst. Ji (Ji et al., 2021) et al. found that an appropriate concentration of N functional groups (2.72 at.%) could maintain the electron-deficient state of Pd, which was conducive to improving H_2O_2 productivity.

N-doped porous carbon was concerned with potential support for the direct synthesis of H_2O_2 from H_2 and O_2. However, the current experimental studies cannot well explain the effect of N functional groups on the synthesis of H_2O_2. To further explore the influence of N functional groups on H_2O_2 directly synthesizing, the method of theoretical calculation relies on the following: (i) constructing Pd/C heterojunctions with different nitrogen contents; (ii) investigating the effect of *N*-doping on the formation energy and electron transfer of Pd/C heterojunctions; (iii) investigating the effect of *N*-doping on O_2 and H_2O_2 adsorption, and O—O bond dissociation. Theoretical calculations showed that *N*-doping could reduce the agglomeration degree of Pd nanoparticles and facilitate electron transfer from carbon support to Pd nanoparticles, which is conducive to the generation of H_2O_2. However, *N*-doping reduced the adsorption energy of O_2 and H_2O_2, the active dissociation energy barrier of O_2, which is detrimental to the desorption of H_2O_2 and the inactive dissociation of O_2, reducing the selectivity of H_2O_2. In order to reduce the adverse effects of *N*-doping, *N*-doped porous carbons with different pore structures were constructed to accelerate the mass transfer and diffusion performance of Pd/C catalyst. The experimental results achieved the expected goal. Compared to other catalysts, the Pd/NPCs-PSS with a highly developed multistage pore structure showed excellent catalytic performance for the direct synthesis of H_2O_2 from H_2 and O_2, the H_2O_2 productivity and selectivity reached 328.4 $mol_{H2O2}{\cdot}kg_{cat}^{-1}{\cdot}h^{-1}$ and 71.9 %, respectively.

2. Computational and experimental

2.1. Computational details

The periodic density functional theory (DFT) calculations of the present work were performed by the CP2K package (Kuhne et al., 2020) with the spin-polarized gradient corrected functional of Perdew Burke and Ernzerhof (PBE) (Perdew et al., 1996). The Goedecker–Teter–Hutter (GTH) pseudopotentials, DZVP-MOLOPT-GTH basis sets were utilized to describe the core electrons and valence electrons (VandeVondele and Hutter, 2007; Goedecker et al., 1996) ($4s^24p^64d^{10}$ for Pd, $2s^22p^4$ for O, $2s^22p^2$ for C, $2s^22p^3$ for N), respectively. 400Ry was set to plane-wave energy cutoff (Lippert and Parrinello, 2010). The electron and force convergence criteria were 1×10^{-6} a.u. and 6×10^{-4} Hartree Bohr, respectively. The transition state of reaction paths was per-

formed using the climbing imagen nudged-elastic-band method (CI-NEB) (Henkelman et al., 2000), including 6 replicas, and the maximum force was 1×10^{-3} atomic units. The transition states had been confirmed by vibrational analysis. The $3 \times 3 \times 1$ Monkhorst–Pack mesh k-points were used for work function calculation. The heterojunction of Pd/-graphite consisted of 4 layers of graphite and 2 layers of Pd (1 1 1) crystal plane. We use VASPKIT (Wang et al., 2021) software 804 functions to automatically generate heterojunction with optimized p(1×1) graphite and Pd(1 1 1)-p(1×1). The mismatch tolerance of heterojunction is less than 1 %. The interlayer space is set to 2.5 Å. The vacuum space was set to 17 Å along the Z-axis. The final periodic box of Pd/-graphite is $9.9 \times 9.9 \times 39.5$ Å. The generated heterojunction model needs to be further optimized before being used. The detailed position information of Pd/graphite heteroatoms is shown in the Supporting Information (Table S5). We replaced carbon atoms with nitrogen atoms in Pd/graphite to build the nitrogen-doped graphite. The adsorption energy (E_{ads}) of O_2 over the Pd/graphite (Pd/*N*-graphite, Pd/2N-graphite) was calculated as below:

$$E_{ads} = E_{O2/slab} - E_{slab} - E_{O2}$$

Where $E_{O2/slab}$ is the total energy of the Pd/graphite (Pd/*N*-graphite, Pd/2N-graphite) slab with the adsorbed atom(O_2); E_{slab} is the total energy of Pd/graphite (Pd/*N*-graphite, Pd/2N-graphite) slab, and E_{O2} is the energy of the O_2 in a box of 9.9 Å × 9.9 Å × 39.5 Å.

The interface formation energy (E_F) of the Pd/graphite (Pd/*N*-graphite, Pd/2N-graphite) was calculated as below:

$$E_F = E_{total} - E_{support} - E_{Pd(111)}$$

Where E_{total} is the total energy of the heterostructure (Pd/-graphite, Pd/*N*-graphite or Pd/2N-graphite). $E_{support}$ is the energy of graphite, *N*-graphite or 2 *N*-graphite, $E_{Pd(1\,1\,1)}$ is the energy of Pd(1 1 1).

The work functions (Φ) of the graphite, *N*-graphite, 2 *N*-graphite and Pd(1 1 1) surfaces according to the following equation:

$$\Phi = E_{vac} - E_F$$

Where E_F is the fermi energy, and E_{vac} is the electrostatic potential of the vacuum level.

The activation barriers and reaction energy were calculated as below:

$$Ea = E_{TS} - E_{IS}$$

$$\Delta E = E_{FS} - E_{IS}$$

E_{IS}, E_{FS} and E_{TS} were the energy of the initial state, final state and transition state.

We used the VASPKIT code (Wang et al., 2021), Multiwfn, (Lu and Chen, 2012) VESTA (Momma and Izumi, 2011) and VMD (Humphrey et al., 1996) for post-processing of the CP2K calculated data.

2.2. Materials

Palladium chloride ($PdCl_2$, 59–60 %), were purchased from Shanghai Aladdin Biochemical Technology Co., ltd; Sodium polyacrylate (MW = 450–700 W, PAANa), Melamine ($C_3H_6N_6$, 99 %), potassium bicarbonate ($KHCO_3$, 99.5 %), Sodium polystyrene sulfonate (MW≈70000, PSS), and Diallyldimethylammonium chloride (PDDA, 60 %) were purchased from Shanghai Macklin Biochemical Co., ltd; glucose ($C_6H_{12}O_6$, 98 %), sodium borohydride ($NaBH_4$, 98 %), ammonium hydroxide ($NH_3{\cdot}H_2O$, 25–28 %) and hydrochloric acid (HCl, 36.0–38.0 %) were purchased from Sinopharm Chemical Reagent Co., ltd; ethanol (C_2H_5OH, 99.7 %) and methanol (CH_3OH, 99.5 %) were purchased from Tianjin Fuyu Fine Chemical Co., ltd. All reagents were used as received without further purification. Deionized water was used throughout the experiment process.

2.3. Catalyst preparation and characterization

The porous carbon (PCs, NPCs, NPCs-PAANa, and NPCs-PSS; the experimental details for porous carbon are given in the Supporting Information) supported Pd catalysts were synthesized by an absorber-reduction method (Fig. 1). In a typical procedure, the porous carbon (100 mg, NPCs-PSS) was added to deionized water (50 ml) on a round flask; after ultrasonication for 30 min, a solution of PDDA (0.5 ml) was added to the mixture and stirred at 35℃ for 24 h. The modified porous carbon was obtained by centrifugation (10000 rpm/min). The modified porous carbon was added to deionized water (50 ml) in a round flask; after ultrasonication for 10 min, a solution of H_2PdCl_4 (0.5 ml, 0.075 M) was added to the mixture and stirred at 35℃ for 24 h. After impregnation, a fresh sodium borohydride solution (1 ml, 10 % wt) was added to the mixture, and the mixture was stirred at 35℃ for 5 h to reduce Pd entirely. The solid was obtained by centrifugation (10000 rpm/min) and dried in air at 80℃ overnight. The dried solid was placed in a tube furnace and treated in the air at 250℃ for 2 h, followed by H_2 reduction at 250℃ for 2.5 h, The sold powder obtained after reduction was named Pd/NPCs-PSS. The experimental details for other catalysts are given in the Supporting Information. Elemental Analyzers, Fourier Transform Infrared Spectrometer (FTIR), Specific surface area and porosity analyzer (ASAP 2460), X-ray diffraction (XRD), Inductively coupled plasma-optical emission spectroscopy (ICP-OES), Raman Spectrometer, scanning electron microscopy (SEM), transmission electron microscopy (TEM) and X-ray photoelectron spectroscopy (XPS) were used to investigate the structure and surface properties of porous carbon and catalyst. The details of the instruments are provided in the Supporting Information.

3. Results and discussion

3.1. Effects of nitrogen doping on the direct synthesis of hydrogen peroxide from hydrogen and oxygen

The first-principles calculations based on density functional theory (DFT) were used to investigate the reaction energetics and atomic interactions within the Pd—N—C metal – carbon heterointerface. The calculations were based on the Pd(1 1 1) crystal plane. Compared with other crystal planes, the Pd (1 1 1) crystal plane is considered the most favorable for the generation of H_2O_2 (Tian et al., 2013). The carbon supports were simplified as graphite, and the doped N atoms exist in graphitic nitrogen. The Pd/C heterojunctions comprised 4 layers of graphite and 2 layers of Pd(1 1 1) crystal plane; further-

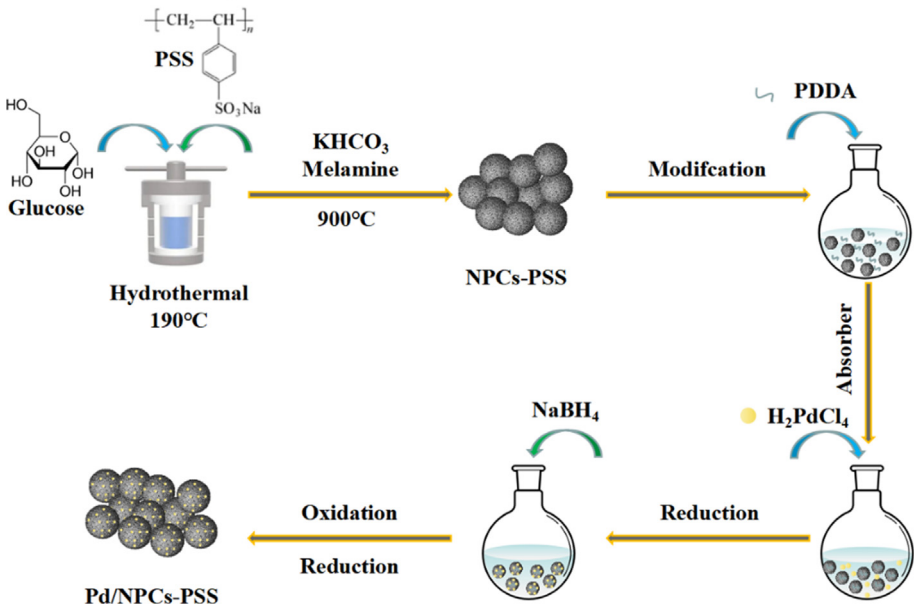

Fig. 1 Schematic diagram of the synthetic route for Pd/NPCs-PSS catalyst.

more, C atoms on the surface of graphite adjacent to the Pd (1 1 1) crystal plane were replaced with N atoms to simulate the Pd—N—C heterojunction. The specific model structures are shown in Fig. S6. The thermodynamic stability of heterojunctions can be described by the interface formation energy (EF). The interface formation energy (EF) of Pd/graphite, Pd/*N*-graphite, and Pd/2N-graphite were − 0.19 eV, −0.81 eV and − 0.97 eV (Table S3), respectively. The negative formation energy indicated that the Pd/graphite, Pd/*N*-graphite, and Pd/2N-graphite could form a stable interface; the Pd/*N*-graphite and Pd/2N-graphite with lower formation energy were conducive to the formation of small Pd nanoparticles, the small Pd nanoparticles were benefited hydrogen peroxide generation (Tian et al., 2017).

The work function of the surface is a crucial parameter to studying charge transfer at the heterojunction interface. The work functions of the graphite, *N*-graphite, 2 *N*-graphite and Pd(1 1 1) surfaces were 4.53 eV, 3.72 eV, 3.68 eV and 5.07 eV (Fig. S7), respectively. The work function of graphite and Pd (1 1 1) surfaces agree with the experimental values of 4.6 eV and 5.3 eV (Oshima and Nagashima, 1997), respectively. As shown in Fig. S6, the fermi energy of Pd(1 1 1) surface was lower than graphite, *N*-graphite and 2 *N*-graphite; when those supports form a heterojunction structure with Pd(1 1 1) surface, electrons will flow from supports to Pd(1 1 1) surface until there have achieved equilibrium in the fermi energies. The interactions and electronic structure between Pd(1 1 1) surface and supports were investigated by calculating differential charge density. Compared with Pd/graphite, the electron density of C atoms on the surface of Pd/*N*-graphite and Pd/2N-graphite disappears, and the electrons are concentrated around Pd and N atoms (Fig. 2). It can be inferred that the graphitic nitrogen in the carbon support promotes the release of electrons from the support to Pd(1 1 1) layer, thereby exhibiting an electron transfer effect.

Bader charge analysis was performed on the Pd/graphite, Pd/*N*-graphite and Pd/2N-graphite heterojunction models to quantify charge transfer at the interfaces. Bader change analysis results show that the amount of charge transfer from graphite, *N*-graphite and 2 *N*-graphite to the Pd(1 1 1) surface were 0.02 e, 0.49 e and 0.48 e, respectively. The plane-average electron difference and the electron displacement curve (Fig. S8) give the same conclusion. The transfer of electrons from *N*-graphite (2 *N*-graphite) to Pd(1 1 1) was conducive to maintaining a high concentration of Pd^0 sites on the surface of Pd(1 1 1). Pd^0 active site could promote the dissociation of H_2 and the activation of O_2, which was beneficial to hydrogen peroxide generation. However, excess Pd^0 active sites will accelerate the dissociation of the O—O bond in O_2 and H_2O_2, resulting in decreased H_2O_2 selectivity.

In the reaction mechanism of the direct synthesis of H_2O_2 from H_2 and O_2, the adsorption and activation of molecular oxygen on the surface of Pd were significant steps (Nugraha et al., 2017). The adsorption energy of O_2 on the surface of Pd/2N-graphite, Pd/*N*-graphite and Pd/graphite were − 0.86 e V, −0.83 eV and − 0.82 eV (Table S3), respectively; indicating that the Pd supported on the *N*-doped carbon surface is beneficial to the adsorption of O_2. The O—O bond length of O_2 after adsorption ranged from 1.38 to 1.39 Å (Table S3) and was higher than in the gas phase. According to the differential charge density figure (Fig. S9), we can indicate that the electrons of the adsorbed O_2 molecules are transferred from Pd atoms and O—O bond to the oxygen atoms, and weakens the O—O bond. The d-Projected density of states (PDOS) of Pd (Fig. S10) were calculated to investigate the influence of *N*-doped on the D-band center of Pd. It is found that with the increase of nitrogen content, the D-band center of Pd was closer to the Fermi level (Fig. S10); according to the D-band center theory, the closer the D-band center of the metal catalyst to the Fermi level, the higher the metal surface activity and the stronger the adsorption of reactants. As the D-band center of Pd approaches the Fermi level, the adsorption energy of O_2 and H_2O_2 decreases from − 0.82 eV to − 0.86 eV and − 0.38 eV to − 0.40 eV (Fig. 3a-b), respectively, the lower adsorp-

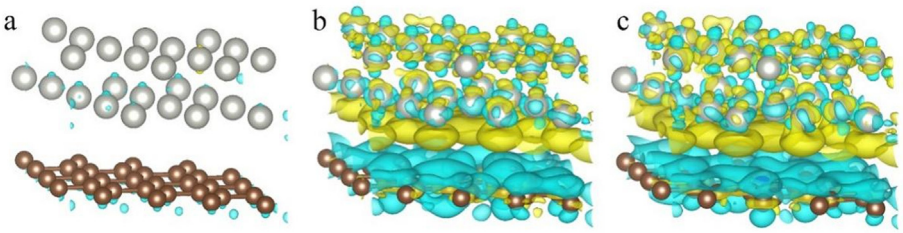

Fig. 2 Differential charge densities of Pd/graphite (a), Pd/*N*-graphite (b) and Pd/2N-graphite (c); Yellow and cyan isosurfaces (±0.0027 $Bohr^{-3}$) show the electron gain and electron loss, respectively.

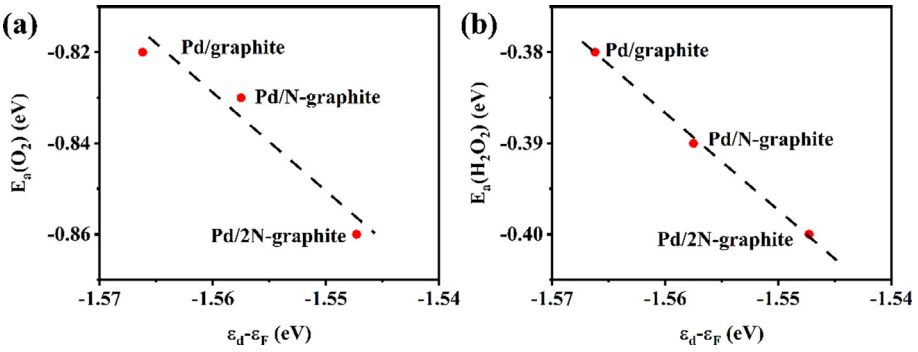

Fig. 3 (a) Adsorption energy of O_2 on Pd/graphite, Pd/*N*-graphite and Pd/2N-graphite, (b) Adsortioon energy of H_2O_2 on Pd/graphite, Pd/*N*-graphite and Pd/2N-graphite.

tion energy was unfavorable for the desorption of O_2 and H_2O_2. As shown in Fig. 4, the activation barriers (Ea) of O_2 dissociation on Pd(1 1 1) surface decreased from 0.53 eV (Pd/-graphite) to 0.49 eV (Pd/*N*-graphite) and 0.48 eV (Pd/2N-graphite). As mentioned above, N doping could reduce oxygen adsorption and dissociation energy (E_a) on Pd(1 1 1) surface, making oxygen more prone to active dissociation. In the reaction mechanism of hydrogen–oxygen synthesis of hydrogen peroxide, the active dissociation of O_2 is not conducive to the generation of hydrogen peroxide. The reactive dissociation of O* reacts with H* to produce the by-product H_2O, resulting in the loss of intermediates, which should be avoided as much as possible in the direct hydrogen–oxygen synthesis of hydrogen peroxide.

The theoretical calculations showed that N doping could reduce the formation energy of Pd/graphite heterojunction; promote the transfer of electrons from carbon supports to Pd particles, which are beneficial to the generation of Pd nanoparticles with a high Pd^0/Pd^{2+} ratio and small particle size. Smaller Pd nanoparticles and a higher proportion of Pd^0 have a favorable effect on H_2O_2 production. However, N doping reduces the adsorption energy of O_2 and H_2O_2, and the dissociation activation barriers of O_2*, which is not conducive to improving H_2O_2 selectivity.

3.2. Porous carbon characterization

In order to suppress the adverse effect of N doping on H_2O_2 synthesis, a series of Pd/C catalysts were fabricated by adjusting the carbon support pore structure. Firstly, *N*-doped porous carbon with high specific surface area and hierarchical pore structure were prepared by one-step multiple activation synthesis techniques. The different precursors produced by the hydrothermal treatment of glucose have undergone a one-step multiple activation process, in which potassium bicarbonate was the pore-forming agent, and melamine was the pore-

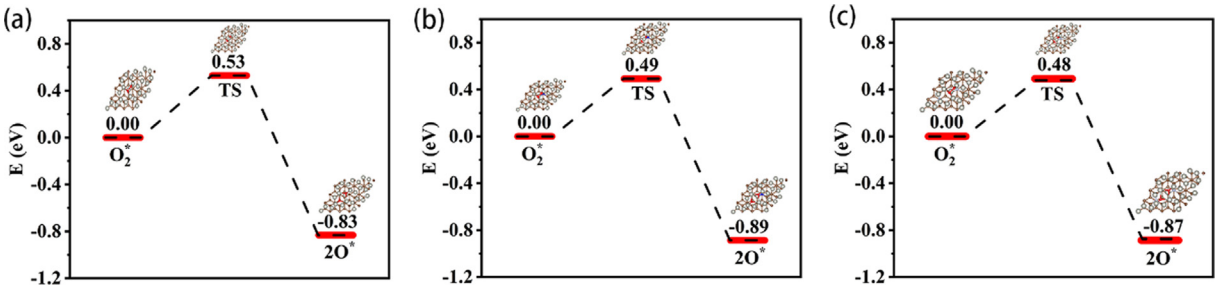

Fig. 4 Energy diagrams for O_2 dissociation on Pd surface with different support; (a) Pd/graphite; (b) Pd/*N*-graphite; (c) Pd/2N-graphite.

forming agent and source of nitrogen, and simultaneously realized the pore-forming activation and nitrogen doping. Then, the Pd nanoparticles were loaded on porous carbon supports through an absorber-reduction strategy. Finally, the stable Pd/C catalyst was obtained by the further oxidation–reduction heat treatment process.

The morphology and size distribution of porous carbon are shown in Fig. 5. By adjusting the hydrothermal treatment process, the activated hydrothermal carbon has different morphologies and structures. The PCs and NPCs were composed of agglomerated carbon microspheres with an average particle size of 310 nm (Fig. 5a-b, Fig. S1a-b). The NPCs-PAANa prepared by adding trace PAANa dispersants were composed of mono-dispersed porous carbon spheres with an average particle size of 437 nm (Fig. 5c, Fig. S1c) (Gong et al., 2014). The NPCs-PSS prepared by adding trace PSS dispersant were formed by carbon spheres with particle sizes less than 100 nm and a rough surface(Fig. 5d, Fig. S1d) (Gong et al., 2014). All of the activated hydrothermal carbon surfaces have obvious irregular porous structures.

The pore structure of porous carbons were analyzed by nitrogen adsorption–desorption isotherm at 77 K (Fig. 6a-b). The detailed data are displayed in Table 1. According to the IUPAC classification, the isothermal adsorption–desorption curve of PCs showed type Ⅰ, indicating that it was dominated by microporous (Guo et al., 2020). The isothermal adsorption–desorption curves of NPCs and NPCs-PAANA were type Ⅳ, and the nitrogen adsorption capacity increased sharply at low relative pressure P/P_0 less than 0.02 of the N_2 sorption isotherms (Fig. 6a), indicating the presence of microporous, the hysteresis loop at relative pressure P/P_0 of 0.4–0.8 can be classified as H2 hysteresis, indicating the presence of mesoporous (Rio et al., 2020). Similar to NPCs-PAANa and NPCs, NPCs-PSS also has H2 type hysteresis loop, indicating that NPCs-PSS also has a mesoporous structure. However, when the relative pressure P/P_0 of 0.8–1.0, NPCs-PSS still has a surge in adsorption capacity, indicating stacking channels in NPCs-PSS (Gong et al., 2014), which was consistent with the SEM image (Fig. 5d). The specific surface area of porous carbons were calculated by Brunaure-Emmett-Teller (BET) model (Table 1). The specific surface area of PCs, NPCs NPCs-PAANa and NPCs-PSS were 1770 m^2/g, 3421 m^2/g, 3165 m^2/g and 3173 m^2/g, respectively. The difference in specific surface area between PCs and NPCs indicates that the volatile gas generated by high-temperature decomposition of melamine will etch hydrothermal carbon aromatic carbon skeleton, forming more pore structures and larger specific surface area (Li et al., 2019; Xu et al., 2020). The pore volumes of porous carbon were calculated by Barrett-Joyner-Halenda (BJH) model. The total pore volumes and the V_{mic}/V_{total} ratio of PCs, NPCs, NPCs-PAANa and NPCs-PSS were 0.99 cm^3/g, 2.16 cm^3/g, 2.44 cm^3/g and 3.43 cm^3/g, 0.79, 0.36, 0.31 and 0.36, respectively. The V_{mic}/V_{total} ratio of porous carbon indicates that the NPCs, NPCs-PAANA and NPCS-PSS have microporous and mesoporous structures. Fig. 6b shows that all of the porous carbons have micropores and mesoporous structures; micropores dominate the pore structure of PCs. In contrast, NPCs and NPCs-PAANa are dominated by meso-

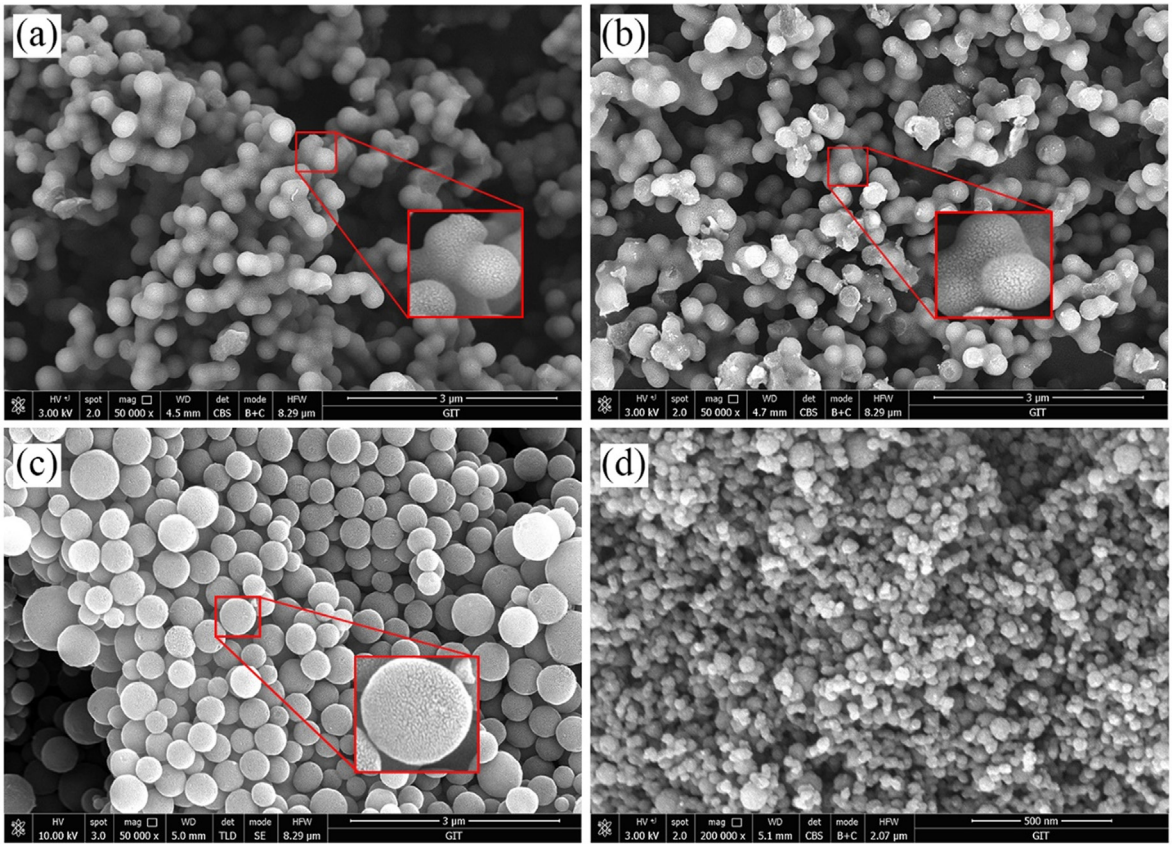

Fig. 5 SEM images of different porous carbon. (a) PCs, (b) NPCs, (c) NPCs-PAANa, (d) NPCs-PSS.

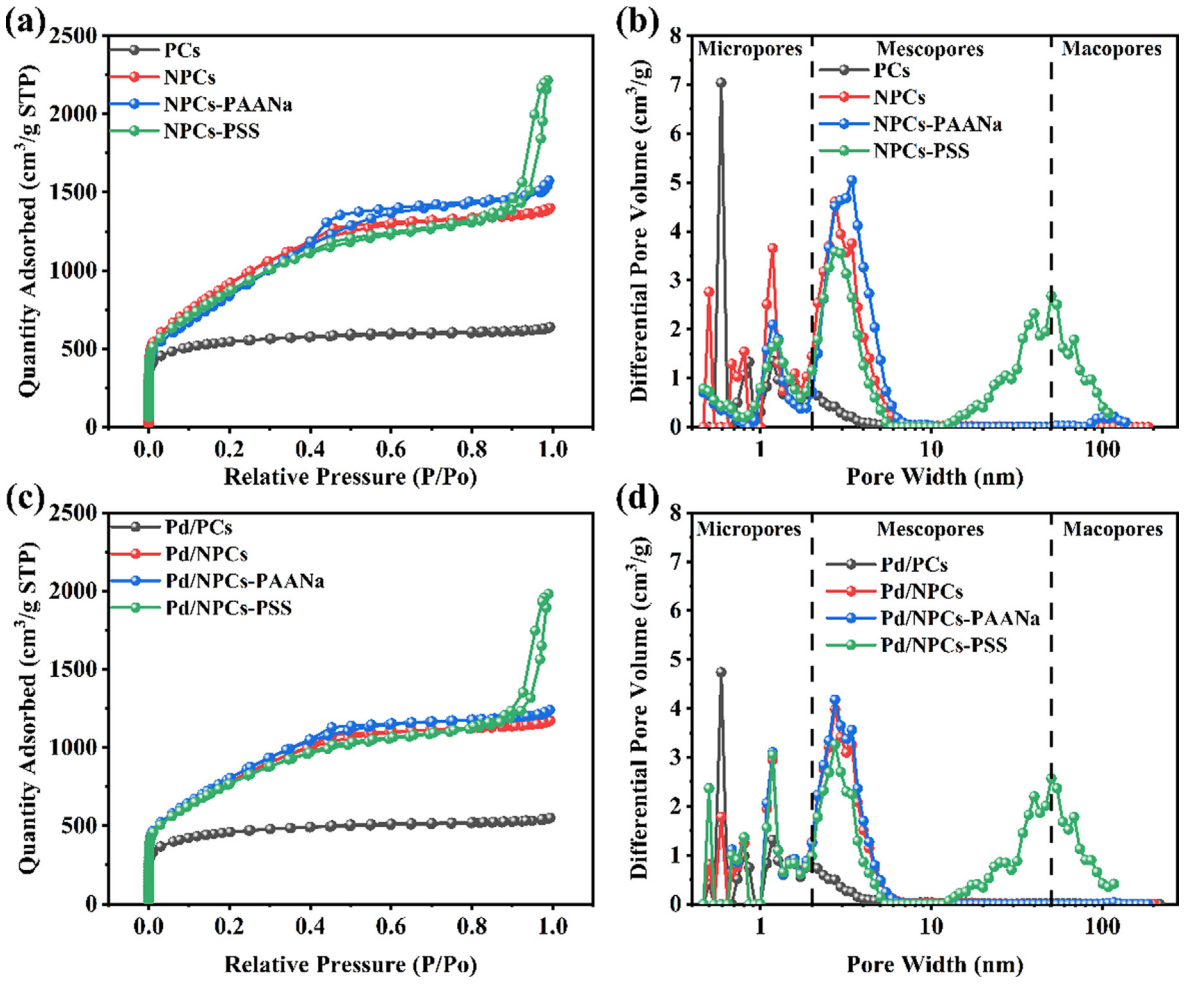

Fig. 6 (a) N_2 adsorption–desorption isotherm of PCs, NPCs, NPCs-PAANa and NPCs-PSS; (b) pore size distribution of PCs, NPCs, NPCs-PAANa and NPCs-PSS using the DFT model; (c) N_2 adsorption–desorption isotherm of Pd/PCs, Pd/NPCs, Pd/NPCs-PAANa and Pd/NPCs-PSS; (d) pore size distribution of Pd/PCs, Pd/NPCs, Pd/NPCs-PAANa and Pd/NPCs-PSS using the DFT model.

Table 1 Textural properties derived from the N_2 adsorption–desorption isotherm.

Samples	S^a_{BET} m^2g^{-1}	Total pore Volume[b] cm^3g^{-1}	V_{mic}/V^c_{total}	Average pore diameter[d] nm
PCs	1770	0.99	0.79	2.23
NPCs	3421	2.16	0.36	2.53
NPCs-PAANa	3165	2.44	0.31	3.08
NPCs-PSS	3173	3.43	0.36	4.17
Pd/PCs	1517	0.85	0.76	2.25
Pd/NPCs	2915	1.81	0.37	2.49
Pd/NPCs-PAANa	2742	1.92	0.34	2.80
Pd/NPCs-PSS	2839	3.06	0.23	4.32

[*a] Specific surface area of porous carbons and Pd/C catalysts with different loadings calculated by Brunauer-Emmertt-Teller (BET) method.
[*b] The total pore volume of porous carbon and Pd/C catalysts with different loadings was calculated from the adsorption amount at $P/P_0 = 0.995$.
[*c] Micropore volume of porous carbon and Pd/C catalysts with different loadings calculated by *t*-Plot model.
[*d] The pore size distribution of porous carbon and different loadings of Pd/C catalysts calculated by density function theory (DFT).

porous with a pore size of 2–5 nm. Besides the similar microporous and mesoporous structures as NPCs and NPCs-PAANa, NPC-PSS has stacked pores with pore diameters of 10–100 nm. The rich mesoporous structure of porous carbon facilitates the mass transfer between catalysts and reactants (Yook et al., 2016).

BET analysis showed that the adjusted glucose hydrothermal process combined with one-step multi-activation strategy

successfully prepared the high specific surface area and high pore capacity carbon supports with micropore-mesoporous and micropore-mesoporous- macroporous multistage pore structures.

The compositions of porous carbons were analyzed by elemental analyzer and XPS. XPS was used to detect the surface composition of the sample. The elemental analyzer was used to determine the contents of C, H, and N in the bulk phase, and the O content was calculated by the difference method. As shown in Table 2, the nitrogen contents of PCs, NPCs, NPCs-PAANa and NPCs-PSS obtained by elemental analyzer were 0.00 %, 0.85 %, 0.74 % and 0.84 % wt%, respectively, consistent with XPS determination, indicating that nitrogen atoms were successfully doped in the surface of porous carbon (Li et al., 2019). The N content of porous carbon obtained by XPS was consistent with the *N*-graphite in the theoretical calculation model.

The samples were subjected to X-ray diffraction (XRD) to analyze the characteristics of carbon crystal structure. As shown in Fig. S12, The diffraction peak of PCs at 2θ values of 44° and 24° can be assigned as the (100) reflection of graphite and (002) reflection of amorphous graphite, respectively (Cai et al., 2020). The intensity of (002) peaks of the NPCs, NPCs-PAANa and NPCs-PSS were lower than the PCs, indicating that the *N*-doped damage the crystal structure of graphite and reduces the graphitization degree. The same conclusion can be obtained from the Raman spectra. As shown in Fig. 7, there are two prominent peaks at $\sim$ 1343 cm^{-1} and $\sim$ 1590 cm^{-1} for these four kinds of porous carbons, which belong to the D and G bands. The D band comes from the crystallization defect in the carbon material, which corresponds to the sp^3 carbon atoms (Wei et al., 2018; Deng et al., 2015); the G band originates from the in-plane vibrations of the SP^2 carbon atoms (Wei et al., 2018; Deng et al., 2015). The intensity ratio of the D band to the G band (I_D/I_G) was used to compare the degree of defects and graphitization in carbon materials (Wei et al., 2018; Deng et al., 2015). The I_D/I_G of NPCs, NPCs-PAANa and NPCs-PSS were higher than PCs, suggesting a more defective structure with lower graphitization. *N*-doped seems to promote the formation of defects in the carbon lattice and reduces the degree of graphitization. The carbon lattice defect sites induced by nitrogen-doped were active due to a reduction in symmetry at or near the crystalline edges (Huang et al., 2021; Zhu et al., 2013).

XPS was used to investigate porous carbon's chemical states of C, N and O elements. According to the C 1 s spectrum of the porous carbons (Fig. S2), three different functional groups such as C—C/C═C (284.8 eV), C—O (286.3 eV) and O-C═O (288.7 eV) were observed. A satellite peak corresponding to the π-π* transition was detected near 290.9 eV, indicating the existence of the graphene-like microstructure on the porous carbon surface (Huang et al., 2020; Shi et al., 2017; Nguyen et al., 2020). The O 1 s spectrum of the porous carbons (Fig. S3) had three different functional groups such as C═O (531.7 eV), O—C—O (533.1 eV) and O-C═O (534.4 eV) (Wu et al., 2021; Cai et al., 2020). The N 1 s spectrum can be divided into four functional groups with different binding energies (Fig. 8); the peak near the binding energy of 398.0 eV, 400.1 eV, 401.4 eV and 403.6 eV are classified into Pyridinic N, Pyrrolic N, Graphitic N and Oxidized N (Arrigo et al., 2016; Wu et al., 2021; Mao et al., 2020; Mao et al., 2019; Jia et al., 2020; Zhang et al., 2020), respectively. According to Table S2, the Graphitic N was the dominant N functional group of NPCs, NPCs-PAANA and NPCS-PSS, and the contents were 40.20 %, 52.04 % and 54.43 %, respectively, which was consistent with the theoretical calculation model.

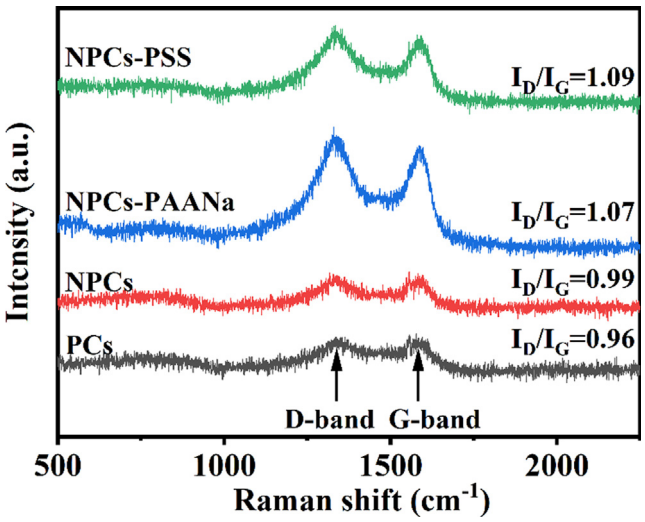

Fig. 7 Raman spectra of porous carbon.

The Fourier transform infrared (FTIR) spectroscopy show that PCs, NPCs, NPCs-PAANa and NPCs-PSS have similar FT-IR spectra (Fig. S13). The broad peaks around 3000 $\sim$ 3600 cm^{-1} could be assigned to the intermolecular hydrogen bonds of carbon and aromatic O—H asymmetry stretching vibration. A small peak around 2926 cm^{-1} could be assigned to the stretching vibrations of $-CH_3$ and $-CH_2$

Table 2 Textural properties of obtained samples.

Samples	C[a]	H[a]	N[a]	O[b]	C[c]	N[c]	O[c]
	(wt%)	(wt%)	(wt%)	(wt%)	(at%)	(at%)	(at%)
PCs	72.20	2.05	–	25.75	81.19	–	10.81
NPCs	89.52	0.78	0.85	8.85	95.35	0.70	2.95
NPCs-PAANa	94.37	0.72	0.74	4.17	96.22	0.66	3.13
NPCs-PSS	88.03	1.03	0.84	10.10	96.04	0.78	3.18

*[a] Obtained by elemental analyzer.
*[b] Calculated by the difference method.
*[c] Obtained by XPS.

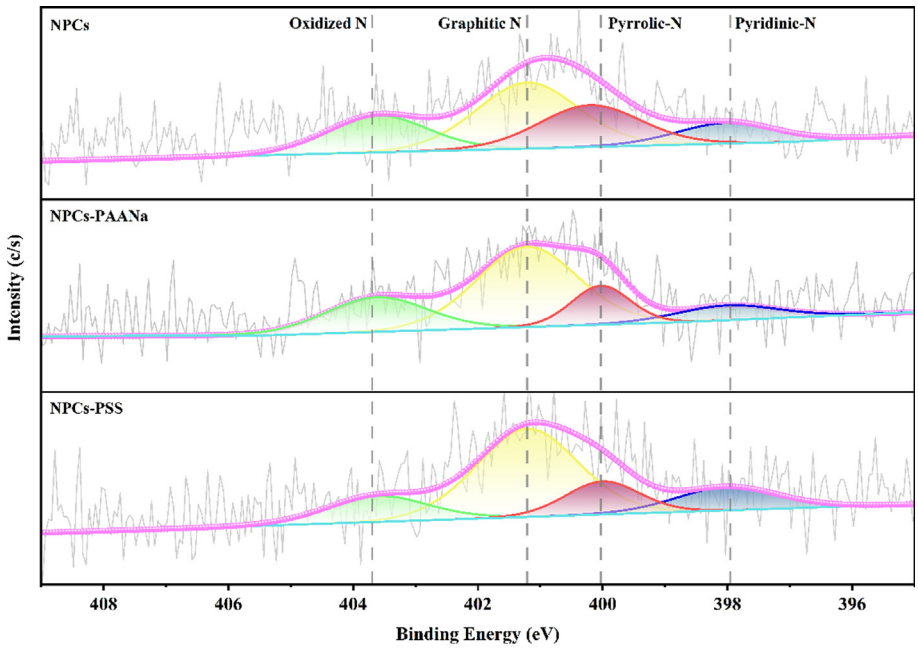

Fig. 8 High-resolution N 1 s spectra of the porous carbon,

groups in aliphatic or cycloalkanes (Sheng et al., 2019). A weaker peak at 1387 cm^{-1} belongs to the stretching vibration of the $–CH_3$ group (Cai et al., 2020; Cuong et al., 2020). The characteristic peaks at 1580 cm^{-1} and 1178 cm^{-1} belonged to vibrational stretching of C═C and C─O in aromatic rings (Chang et al., 2020). No prominent nitrogen-containing groups were found in the FT-IR spectra, which may be related to the low nitrogen content (Gong et al., 2014).

3.3. Catalyst characterization

As shown in Fig. 6c-d, Pd/C catalysts' pore structure, size distribution, specific surface area, and pore volume are consistent with their carbon supports (Table 2), indicating that the Pd/C catalyst prepared by the absorber-reduction method could inherit the structural properties of the porous carbon support. The specific surface area and pore volume of Pd/PCs, Pd/NPCs, Pd/NPCs-PAANa and Pd/NPCs-PSS catalysts were 1517 m^2g^{-1}, 2915 m^2g^{-1}, 2742 m^2g^{-1} and 2839 m^2g^{-1}, and 0.85 cm^3g^{-1}, 1.81 $cm^3g^{-1}$and 3.06cm^3g^{-1}, respectively. The higher specific surface area and pore volume of Pd/NPCs, Pd/NPCs-PAANa and Pd/NPCs-PSS catalysts are beneficial for exposing a high density of active sites and ensuring fast mass transfer.

Fig. 9 displays the XRD patterns of Pd/PCs, Pd/NPCs, Pd/NPCs-PAANa and Pd/NPCs-PSS in the range of 10-90° (2θ). The Pd/PCs have five different peaks; the peaks at 39.92°, 46.43°, 67.76°, 81.64° and 86.12° can be indexed to the (111), (200), (220), (311) and (222) planes of face-centered cubic (fcc) Pd (JCPDS# 87–0643) (Li et al., 2018), respectively. Pd/NPCs, Pd/NPCs-PAANa and Pd/NPCs-PSS have only observed the diffraction peak of the Pd (111) plane and are consistent with the theoretical calculation model. Compared with the Pd (111) peak in Pd/PCs, the intense peak around 40° in Pd/NPCs downshifts by 0.3°, and the full-width half-maximum (FWHM) increases by 0.9° (Fig. S14). The same situation also exists in Pd/NPCs-PAANa and Pd/NPCs-PSS, indicating Pd/NPCs, Pd/ NPCS-PAANa and Pd/ NPCS-PSS may have slight lattice stretching. The average size of Pd nanoparticles of Pd/C catalysts were calculated by the Scherrer formula. The calculated Pd nanoparticles size of Pd/PCs, Pd/NPCs, Pd/NPCs-PAANa and Pd/NPCs-PSS were 14.2 nm, 5.1 nm, 5.5 nm and 3.3 nm, respectively.

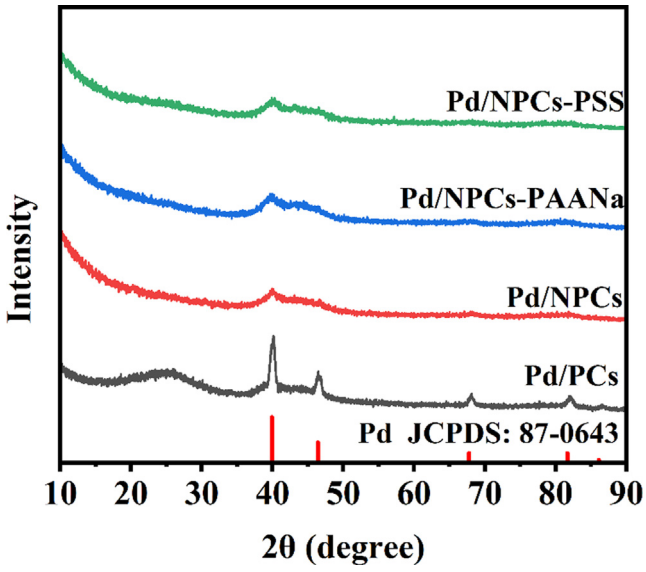

Fig. 9 XRD patterns of Pd/C catalysts.

Fig. 10a-d presents TEM images of Pd/PCs, Pd/NPCs, Pd/NPCs-PAANa and Pd/NPCs-PSS, and it can be observed that Pd nanoparticles are evenly dispersed on the surface of porous carbon. The average particle sizes of Pd nanoparticles on Pd/PCs, Pd/NPCs, Pd/NPCs-PAANa and Pd/NPCs-PSS were 14.9 nm, 4.6 nm, 5.2 nm and 4.2 nm, respectively, agree well

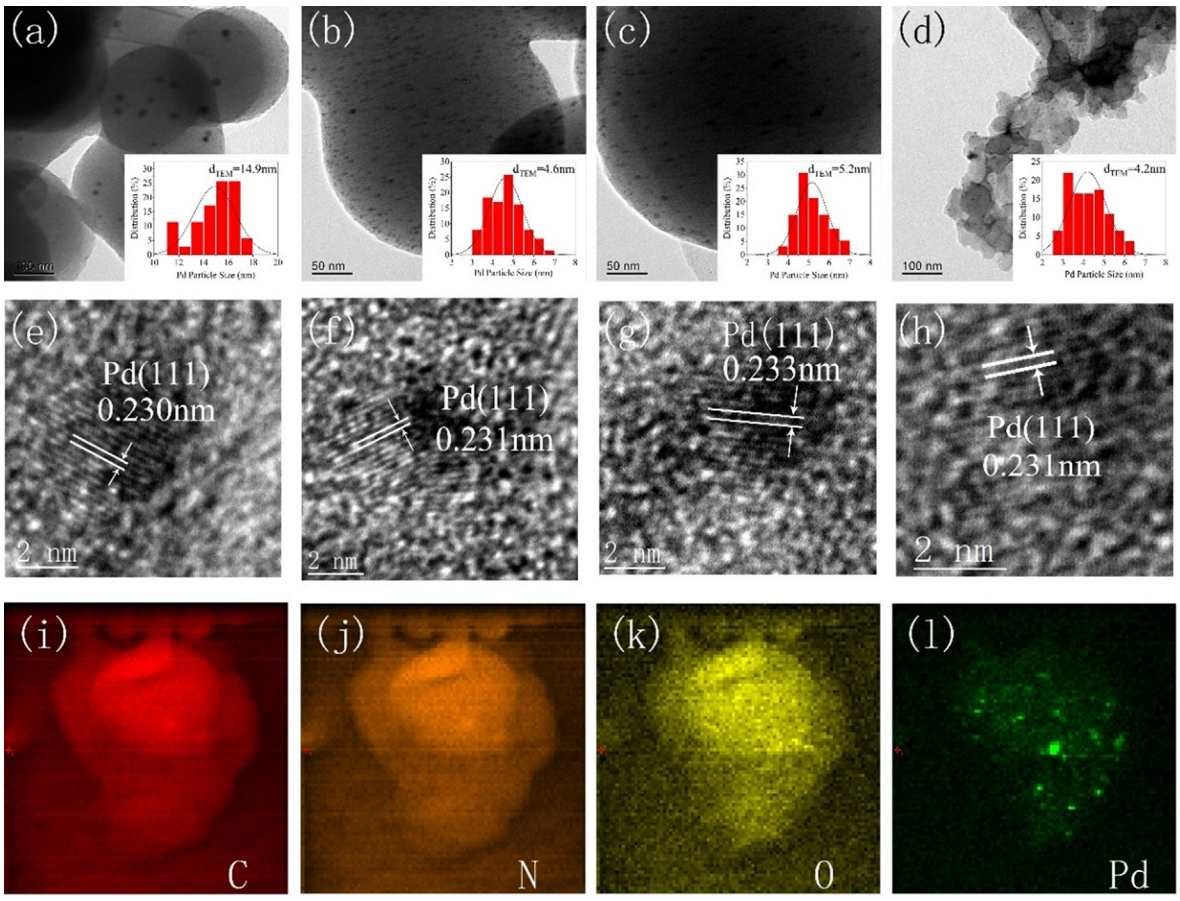

Fig. 10 TEM images of (a) Pd/PCs, (b) Pd/NPCs, (c) Pd/NPCs-PAANa, (d) Pd/NPCs-PSS; the HR-TEM images of (e) Pd/PCs, (f) Pd/NPCs, (g) Pd/NPCs-PAANa, (h) Pd/NPCs-PSS; (i) STEM image of Pd/NPCs-PSS and the corresponding mapping images of (j) C, (k) N, (l) O, (m) Pd.

with the XRD results. It is worth noting that the average particle size of Pd nanoparticles was strongly correlated with the concentration of N functional groups of the porous carbon (Fig. S5). The average particle size of Pd nanoparticles in nitrogen-containing porous carbons (NPCs, NPCs-PAANa and NPCs-PSS) was smaller than *N*-free porous carbons (PCs) and negatively correlated with the nitrogen concentration, which is consistent with the theoretical calculation results. Theoretical calculation shows that the formation energy of Pd/C heterojunction was significantly reduced with nitrogen doping and further reduced with increased nitrogen content. The lower formation energy is conducive to anchoring Pd nanoparticles on the surface of the porous carbon support, inhibiting the agglomeration of Pd nanoparticles during redox heat treatment, and facilitating the formation of small particle-size Pd nanoparticles. The smaller Pd particle size could increase hydrogen peroxide production (Tian et al., 2017). The lattice spacing of Pd(1 1 1) in Pd/NPCs (0.231 nm), Pd/NPCs-PAANa (0.233 nm) and Pd/NPCs-PSS (0.231 nm) were slightly larger than that of Pd/PCs (0.230 nm) (Fig. 10e-h), agree well with the XRD results. Energy-dispersive X-ray spectroscopy (EDS) elemental mapping Fig. 10i-k showed that the C, N and O atoms were uniformly distributed on the NPCs-PSS support. It is beneficial for the dispersion of the Pd nanoparticles (Fig. 10*l*).

The electronic state of Pd and N atoms was further researched by Pd 3d and N 1 s X-ray photoelectron spectroscopy (XPS). Fig. 11 shows that the complex Pd 3d was deconvoluted into four different peaks with the binding energies of Pd^0 (~341 eV, ~335 eV) and Pd^{2+} (~343 eV, ~337 eV) (Liang et al., 2020; Thuy Vu et al., 607 (2020).). These results indicated that the Pd^{2+} exited in all catalysts, even though the catalysts were heat treatment in the hydrogen atmosphere. It was worth noting that the binding energies of Pd^0 (Table S2) decreased in the order of Pd/PCs (335.83 e V) > Pd/NPCs (335.80 eV) = Pd/NPCs-PAANa (335.80 e V) > Pd/NPCs-PSS(335.72 eV), suggesting that N doping can facilitate electron flow from the porous carbon support to the supported Pd nanoparticles (Li et al., 2019), theoretical calculations can infer the same result. Benefiting from electron transfer, the Pd/NPCs, Pd/NPCs-PAANa and Pd/NPCs-PSS have a higher Pd^0/Pd^{2+} ratio than the Pd/PCs (Table S2). The nitrogen species of catalysts were the same as their supports, but the content was reduced (Table S1), possibly because Pd nanoparticles cover part of the N sites.

The above evidence confirms that nitrogen doping can effectively inhibit the agglomeration of Pd nanoparticles and promote the Pd nanoparticles to obtain electrons from the *N*-dope porous carbon support, which is consistent with the theoretical calculation results.

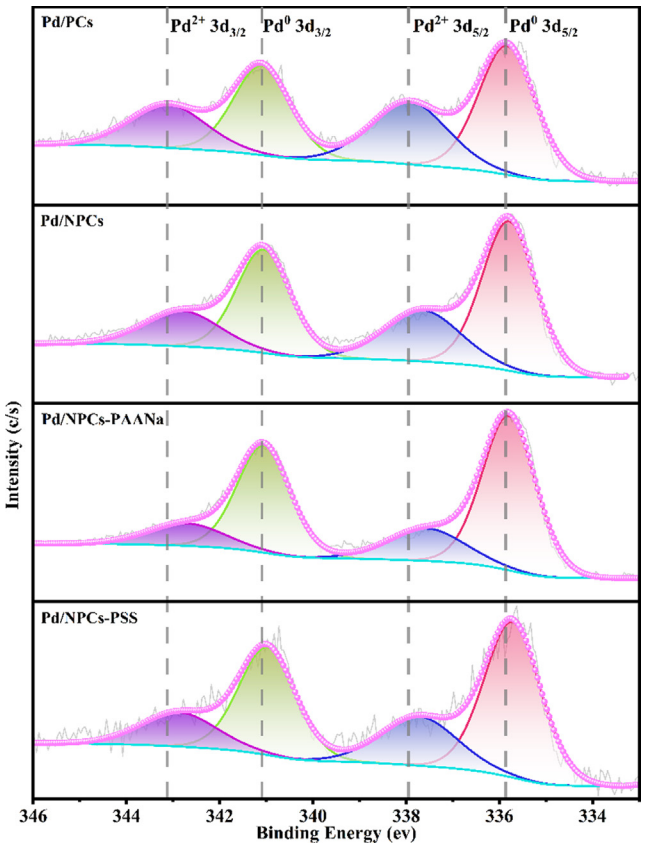

Fig. 11 High-resolution Pd 3d spectra of the Pd/C catalysts.

3.4. Catalytic performance evaluation of Pd/C catalysts for the direct synthesis of hydrogen peroxide from hydrogen and oxygen

Fig. 12 shows the change of catalytic performance with the time of different Pd/C catalysts for the direct synthesis of hydrogen peroxide. During the reaction period (3.0 h), the concentration of hydrogen peroxide in the solution increased (Fig. 12a), indicating that all the catalysts maintained high activity throughout the reaction. Compared with the Pd/PCs, the Pd/NPCs supported by *N*-doped porous carbon have higher hydrogen peroxide productivity (Fig. 12b) and hydrogen conversion rate (Fig. 12c) but lower hydrogen peroxide selectivity (Fig. 12d); the experimental result agrees well with the conclusion of theoretical calculations. According to Fig. 12, there are two points worth noting: (i) at the beginning of the reaction (0.5 h), the hydrogen conversion rate was positively correlated with the Pd^0/Pd^{2+} ratio (Table S2), and the Pd/NPCs-PAANa had the highest hydrogen conversion rate. An hour later, the hydrogen conversion rate of Pd/NPCs-PSS exceeded the Pd/NPCs-PAANa (Fig. 12c); (ii) the catalysts (Pd/NPCs, Pd/NPCs-PAANa, and Pd/NPCs-PSS) showed observed differences in H_2O_2 selectivity. The Pd^0/Pd^{2+} ratio of Pd/NPCs-PSS fall in between Pd/NPCs and Pd/NPCs-PAANa; however, the Pd/NPCs-PSS had the highest hydrogen peroxide selectivity and productivity (Fig. 12d);

The size of Pd nanoparticles is one of the factors affecting the direct synthesis of hydrogen peroxide by hydrogen and oxygen. Han's (Tian et al., 2017) research showed that H_2O_2 selectivity is strongly correlated with particle size when the particle size of Pd nanoparticles is 1.4–2.5 nm, and the effect of particle size on H_2O_2 selectivity is slight when the particle size is 2.5–30 nm. According to the Fig. 10, the average particle sizes of Pd nanoparticles on Pd/PCs, Pd/NPCs, Pd/NPCs-PAANa and Pd/NPCs-PSS were 14.9 nm. 4.6 nm, 5.2 nm and 4.2 nm, respectively, especially for Pd/NPCs, Pd/NPCs-PAANa and Pd/NPCs-PSS with average particle size between 4.2 nm and 5.2 nm. Therefore, the effect of particle size on the catalytic properties of Pd/NPCs, Pd/NPCs-PAANa and Pd/NPCs-PSS can be ignored in this study. The Pd^0/Pd^{2+} ratio of Pd nanoparticles is another important factor affecting the direct synthesis of hydrogen peroxide (Edwards et al., 2012). Pd^0 is the main active site of H_2 dissociation, Pd^{2+} could inhibit the dissociation of H_2O_2 and improve the H_2O_2 selectivity. The Pd^0/Pd^{2+} ratios of Pd/PCs, Pd/NPCs, Pd/NPCs-PAANa and Pd/NPCs-PSS were 1.53, 2.07, 3.33 and 2.35 (Table S2), respectively. A higher Pd^0/Pd^{2+} ratio indicated a higher H_2 conversion and a lower H_2O_2 selectivity. At the initial stage (0.5 h), Pd/NPCs-PAANa showed the highest H_2 conversion, while H_2O_2 selectively decreased in the order of Pd/PCs > P d/NPCs > Pd/NPCs - PAANa. Although the difference of Pd^0/Pd^{2+} ratio could partly explain point (i) and point (ii), it does not explain the abnormality at point (i) and point (ii). We believe that there are other factors affecting the catalytic performance of hydrogen peroxide. Earlier research suggested that the mesoporous structure of porous carbon could alter the H_2O_2 selectivity by affecting the mass transfer within the catalyst (Yook et al., 2016; Park et al., 2014; Fellinger et al., 2012). Compared with Pd/PCs, the Pd^0 content of Pd/NPCs was increased 7 %, and the H_2 conversion was increased 17 %. Compared with Pd/NPCs, the Pd^0 content of Pd/NPCs-PAANa was increased 9.5 %, and the H_2 conversion only increased 3.1 %. These results imply that compared with the microporous structure, the mesoporous structure is more conducive to the diffusion of H_2 in the catalyst and improved H_2 conversion, which is consistent with Choi (Yook et al., 2016). After an hour of reaction, the H_2 conversion of Pd/NPCs, Pd/NPCs-PAANa and Pd/NPCs-PSS were 63.0 %, 66.1 % and 66.4 %, respectively, and with a decrease of 7.9 %, 7.9 % and 5.8 %, respectively. The slow decline rate of Pd/NPCs-PSS may be related to the particular pore structure. Compared with Pd/NPCs-PAANa, the larger average pore size and the higher mesoporous ratio of Pd/NPCs-PSS are more conducive to H_2 mass transfer in the catalyst and improve H_2 conversion.

According to the mechanism of direct synthesis of hydrogen peroxide (Han et al., 2021), O—O bond dissociation is the key that affects the selectivity of H_2O_2. A lower Pd^0 content is beneficial for improving the selectivity of hydrogen peroxide. At the initial stage (0.5 h), H_2O_2 selectivity was negatively correlated with Pd^0 content, except Pd/NPCs-PSS. The H_2O_2 selectivity of Pd/NPCs-PSS was up to 78.8 %, indicating that other factors may affect the H_2O_2 selectivity. The solution does not contain hydrogen peroxide at the beginning of the reaction, the dissociation of O_2 has an important effect on the hydrogen peroxide selectivity. Xu and co-worker studied (Tian et al., 2020) that the selectivity of hydrogen peroxide is facilitated when O co-adsorbed on the surface of Pd. The Pd/PCs, Pd/NPCs, and Pd/NPCs-PAANa have similar pore structures and average pore diameters, resulting in no significant difference in the diffusion of O_2 within these catalysts. The

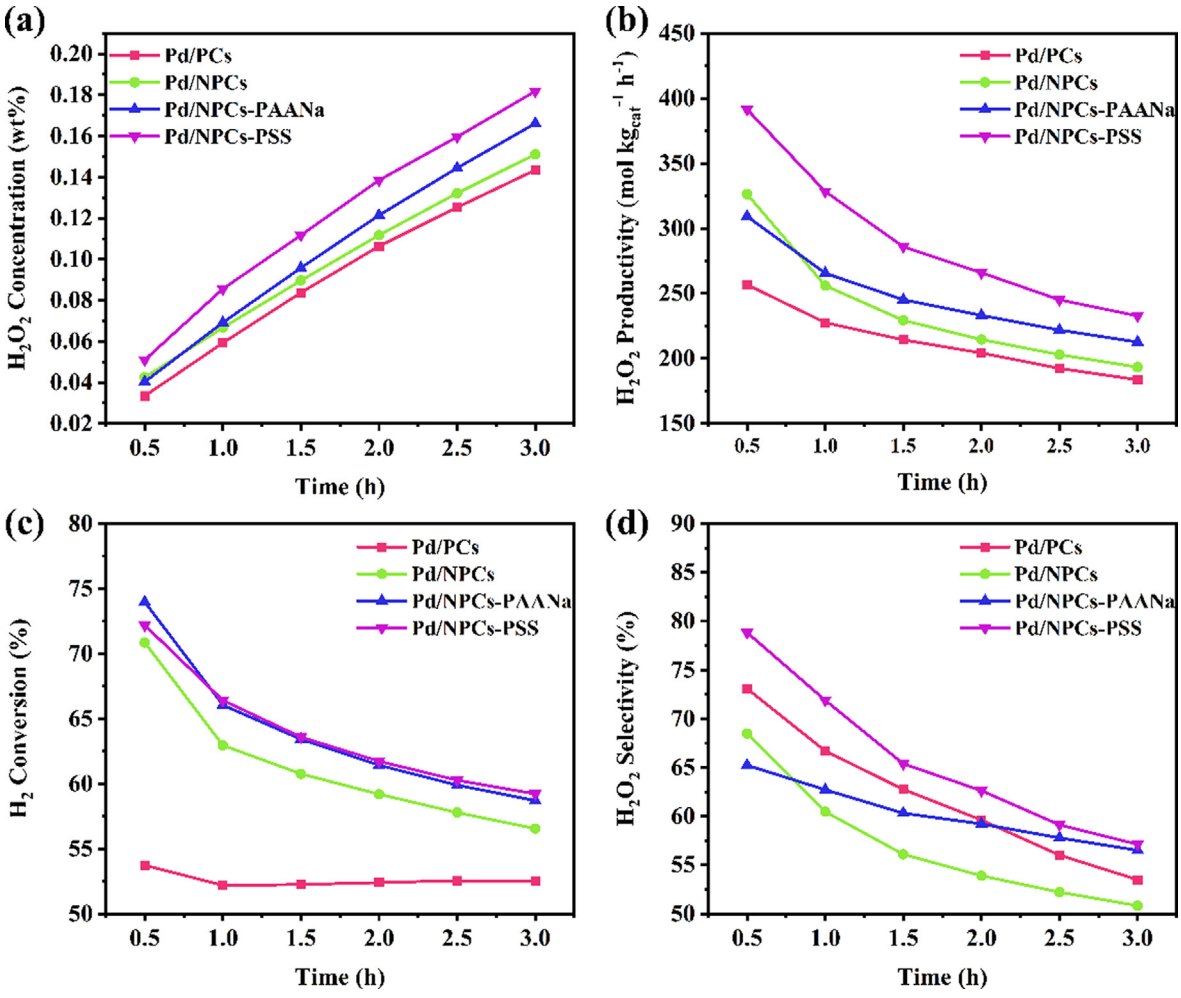

Fig. 12 Direct synthesis of H_2O_2 using various Pd/C catalysts (reaction conditions: catalyst 10 mg, 160 ml MeOH, 1.8 ml 98 wt% H_2SO_4, total flow rate 16.25 ml/min at atmosphere, H_2:O_2:N_2 = 2.25:4:10, 120 rpm/min, 273.15 K, 3.0 h.) (a) H_2O_2 concentration, (b) H_2O_2 productivity, (c) H_2 conversion, (d) H_2O_2 selectivity.

Pd/NPCs-PSS has a special macropore-mesoporous structure and average pore diameters up to 4.32 nm, which could promote the mass transfer of O_2 in the catalyst. The good mass transfer of O_2 leads to the faster co-adsorption equilibrium of O on the Pd surface, which improves hydrogen peroxide selectivity. As the reaction progress, the concentration of hydrogen peroxide in the solution gradually increases (Fig. 12a), and the dissociation of hydrogen peroxide becomes an essential factor affecting the catalytic performance. Kakimoto's research (Park et al., 2014) showed that the porous carbon's mesoporous structure could improve the catalyst layer's mass transfer and reduce the contact time of H_2O_2 inside the catalyst, thereby reducing the decomposition of H_2O_2. In addition to a large number of 2–5 nm mesopores, the Pd/NPCs-PSS also had a large number of 10–100 nm mesopores-macropores. The mesopores-macropores structure enhanced the mass transfer of H_2O_2, reduced the residence time of H_2O_2 in the catalyst, and improved the selectivity of H_2O_2.

In addition to the above, two other points are worth noting here, (i). the H_2O_2 selectivity of Pd/NPCs-PAANa exceeded the Pd/NPCs after reaction an hour, and the difference tended to expand (Fig. 12d); (ii) the difference in H_2O_2 selectivity between Pd/NPCs-PAANa and Pd/NPCs-PSS gradually decreased as the reaction progressed (Fig. 12d). After fully investigating the effect of Pd nanoparticle size, the surface electronic state of Pd and the pore structure of the catalyst support, these two points seem to imply that the dispersion of the catalyst support also has the potential to affect the selectivity of hydrogen peroxide, which worth to research in the future.

Table S4 compares the catalytic performance of Pd/NPCs-PSS catalysts with other carbon-supported Pd-based catalysts. At ambient pressure, the hydrogen peroxide productivity and selectivity of Pd/NPCs-PSS were up to 328.4 mol_{H2O2} $kg_{cat}^{-1}h^{-1}$ and 71.9 %., respectively. The excellent catalytic performance of Pd/NPCs-PSS indicates that *N*-doped porous carbon with a macropore-mesoporous-microporous structure is an excellent material for directly synthesizing hydrogen peroxide from hydrogen and oxygen.

3.5. Hydrogen peroxide decomposition and hydrogenation test

A series of experiments were performed to study the influence of Pd/C catalysts on the hydrogenation and decomposition of hydrogen peroxide. According to Fig. 13, the hydrogenation rates of Pd/C catalysts are higher than the decomposition

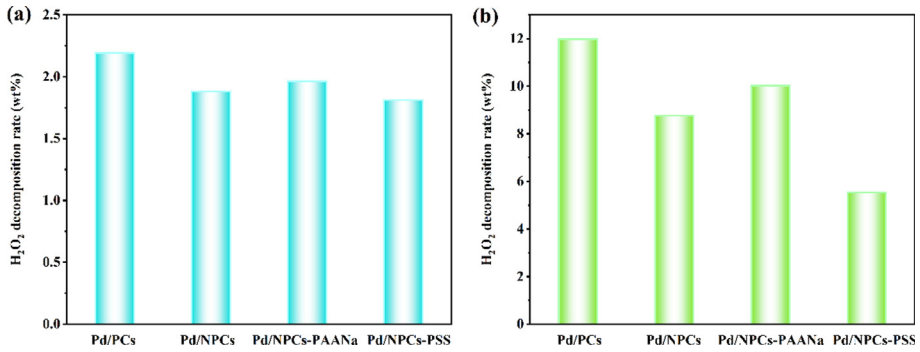

Fig. 13 (a) H_2O_2 decomposition of different catalysts; (b) H_2O_2 hydrogenation of different catalysts (reaction conditions: catalyst 10 mg, 160 ml MeOH, 1.8 ml 98 wt% H_2SO_4, 120 rpm/min, 273.15 K, 1.0 h, H_2O_2 decomposition test the flow rate of N_2 is10 ml/min; H_2O_2 hydrogenation test the flow rate of N_2 is10 ml/min, the flow of H_2 is 2.25 ml/min).

rates, which indicates that hydrogenation was the primary side reaction (Thuy Vu et al., 607 (2020).; Tian et al., 2020). It is worth noting that Pd/NPCs-PSS had the lowest dissociation and hydrogenation rates than Pd/NPCs and Pd/NPCs-PAANa; although Pd/NPCs-PSS has the smallest Pd particle size (Fig. 10d), the difference in metal particle size distribution too small to fully explain the substantial difference in catalytic results. Therefore, we believe that the pore structure of the catalyst support (Fig. 6 b) also influences hydrogen peroxide's hydrogenation and dissociation performance. The unique macropore-mesoporous-micropore structure of the Pd/NPCs-PSS catalyst reduced hydrogen peroxide's dissociation and hydrogenation rates by increasing the diffusion rates of hydrogen and hydrogen peroxide in the catalyst.

3.6. Catalyst recycling

Reusability is an important property of the catalyst. In-cycle tests were performed on Pd/NPCs-PSS to examine the stability and reusability of the catalyst. After being reused two times, the H_2 conversion, H_2O_2 selectivity and productivity decreased (Fig. S15). ICP, XRD and XPS were used to analyze the Pd invasion, geometry and electronic morphology of Pd/NPCs-PSS after rescue. The ICP analysis of Pd/NPCs-PSS before and after circulation implied that the leaching of Pd during the catalyst recycling could be negligible (Table S2). the XPS analysis of Pd/NPCs-PSS after circulation implied that the catalyst recycling could reduce the Pd^0 content (Fig. S16). The XRD analysis of Pd/NPCs-PSS shows that the catalyst recycling changed Pd's morphology and particle size. The crystal plane, unsuitable for H_2O_2 production, can be observed in the XRD pattern (Fig. S17), such as the (100) crystal plane. The average particle size of Pd calculated by the Scherrer formula was 16.2 nm implying that Pd agglomerated in catalyst cycling.

4. Conclusions

In summary, guided by theoretical calculations, we prepared a series of Pd/C catalysts comprising highly dispersed Pd nanoparticles deposited onto hierarchically porous nitrogen-doped carbon material to efficiently synthesize hydrogen peroxide from hydrogen and oxygen. DFT results indicated that the N doping reduces the formation energy of Pd/C heterojunction, promoting the transfer of electrons from carbon support to Pd nanoparticles, forming Pd nanoparticles with small particle size and high Pd^0/Pd^{2+} ratio, and beneficial to improving the hydrogen peroxide productivity. However, N doping shifts the D-band center of Pd toward the Fermi level, and lowers the active dissociation energy barrier of O_2, which reduces hydrogen peroxide selectivity. The experimental results showed that adjusting the pore structure of the *N*-doped porous carbon supports could reduce the negative effect of N doping for H_2O_2 selectivity. Compared with other catalysts, the special pore structure of Pd/NPCs-PSS catalyst improved the mass transfer rate of H_2, O_2 and H_2O_2 in the catalyst, which was the key to inhibiting the negative effects of N doping. At ambient pressure, the hydrogen peroxide productivity and selectivity of Pd/NPCs-PSS were up to 328.4 $mol_{H2O2}{\cdot}kg_{cat}^{-1}{\cdot}h^{-1}$ and 71.9 %, respectively. This study provides a possible solution to design high-performance Pd/C catalysts to directly synthesize hydrogen peroxide from hydrogen and oxygen at atmospheric pressure.

Declaration of Competing Interest

The authors declare that they have no known competing financial interests or personal relationships that could have appeared to influence the work reported in this paper.

Acknowledgments

Thanks for the computing support of the State Key Laboratory of Public Big Data, Guizhou University. This work was financially supported by National Natural Science Foundation of China, China (Grant No.22068009), Natural Science Basic Research Program of Guizhou Province, China (Grant No. ZK[2022]088), Cultivation Project of Guizhou University, China (Grant No. [2020]38). the Open Project of Guizhou University Laboratory and Equipment Departments, China (No.SYSKF2022-045) and College Students innovation and entrepreneurship training program of Guizhou Institute of Technology, China (No.S202014440090)

Appendix A. Supplementary material

Supplementary data to this article can be found online at https://doi.org/10.1016/j.arabjc.2022.104452.

References

Abate, S., Arrigo, R., Schuster, M.E., Perathoner, S., Centi, G., Villa, A., Su, D., Schlögl, R., 2010. Pd nanoparticles supported on N-

doped nanocarbon for the direct synthesis of H2O2 from H2 and O2. Catal. Today 157, 280–285.
Agarwal, N., Thomas, L., Nasrallah, A., Sainna, M.A., Freakley, S.J., Edwards, J.K., Catlow, C.R.A., Hutchings, G.J., Taylor, S.H., Willock, D.J., 2021. The direct synthesis of hydrogen peroxide over Au and Pd nanoparticles: A DFT study. Catal. Today 381, 76–85.
Arrigo, R., Schuster, M.E., Abate, S., Wrabetz, S., Amakawa, K., Teschner, D., Freni, M., Centi, G., Perathoner, S., Havecker, M., Schlogl, R., 2014. Dynamics of palladium on nanocarbon in the direct synthesis of H2O2. ChemSusChem 7, 179–194.
Arrigo, R., Schuster, M.E., Abate, S., Giorgianni, G., Centi, G., Perathoner, S., Wrabetz, S., Pfeifer, V., Antonietti, M., Schlogl, R., 2016. Pd supported on carbon nitride boosts the direct hydrogen peroxide synthesis. ACS Catal. 6, 6959–6966.
Cai, J., Chen, T., Cui, L., Jia, Q., Liu, M., Zheng, R., Yan, G., Wei, D., Liu, J., 2020. A three-dimensional and porous bi-nanospheres electrocatalytic system constructed by in situ generation of Ru nanoclusters inside and outside polydopamine nanoparticles for highly efficient hydrogen evolution reaction. Int. J. Hydrogen Energy 45, 6592–6603.
Chang, Q., Zhang, P., Mostaghimi, A.H.B., Zhao, X., Denny, S.R., Lee, J.H., Gao, H., Zhang, Y., Xin, H.L., Siahrostami, S., Chen, J. G., Chen, Z., 2020. Promoting H2O2 production via 2-electron oxygen reduction by coordinating partially oxidized Pd with defect carbon. Nat. Commun. 11, 2178.
Cuong, D.V., Wu, P.-C., Liu, N.-L., Hou, C.-H., 2020. Hierarchical porous carbon derived from activated biochar as an eco-friendly electrode for the electrosorption of inorganic ions. Sep. Purif. Technol. 242.
Deng, J., Xiong, T., Xu, F., Li, M., Han, C., Gong, Y., Wang, H., Wang, Y., 2015. Inspired by bread leavening: one-pot synthesis of hierarchically porous carbon for supercapacitors. Green Chem. 17, 4053–4060.
Doronkin, D.E., Wang, S., Sharapa, D.I., Deschner, B.J., Sheppard, T.L., Zimina, A., Studt, F., Dittmeyer, R., Behrens, S., Grunwaldt, J.-D., 2020. Dynamic structural changes of supported Pd, PdSn, and PdIn nanoparticles during continuous flow high pressure direct H2O2 synthesis. Catal. Sci. Technol. 10, 4726–4742.
Edwards, J.K., Pritchard, J., Piccinini, M., Shaw, G., He, Q., Carley, A.F., Kiely, C.J., Hutchings, G.J., 2012. The effect of heat treatment on the performance and structure of carbon-supported Au–Pd catalysts for the direct synthesis of hydrogen peroxide. J. Catal. 292, 227–238.
J.K. Edwards, B. Solsona, E.N. N, A.F. Carley, A.A. Herzing, C.J. Kiely, G.J. Hutchings, Switching off hydrogen peroxide hydrogenation in the direct synthesis process, Science, 323 (2009) 1037-1041
Edwards, J.K., Freakley, S.J., Carley, A.F., Kiely, C.J., Hutchings, G. J., 2014. Strategies for designing supported gold-palladium bimetallic catalysts for the direct synthesis of hydrogen peroxide. Acc. Chem. Res. 47, 845–854.
Fellinger, T.P., Hasche, F., Strasser, P., Antonietti, M., 2012. Mesoporous nitrogen-doped carbon for the electrocatalytic synthesis of hydrogen peroxide. J. Am. Chem. Soc. 134, 4072–4075.
Fukuzumi, S., Lee, Y.M., Nam, W., 2021. Recent progress in production and usage of hydrogen peroxide. Chin. J. Catal. 42, 1241–1252.
García, T., Agouram, S., Dejoz, A., Sánchez-Royo, J.F., Torrente-Murciano, L., Solsona, B., 2015. Enhanced H2O2 production over Au-rich bimetallic Au–Pd nanoparticles on ordered mesoporous carbons. Catal. Today 248, 48–57.
Goedecker, S., Teter, M., Hutter, J., 1996. Separable dual-space Gaussian pseudopotentials. Phys. Rev. B Condens. Matter 54, 1703–1710.
Gong, Y., Xie, L., Li, H., Wang, Y., 2014. Sustainable and scalable production of monodisperse and highly uniform colloidal carbonaceous spheres using sodium polyacrylate as the dispersant. Chem. Commun. (Camb.) 50, 12633–12636.
Gong, Y., Wei, Z., Wang, J., Zhang, P., Li, H., Wang, Y., 2014. Design and fabrication of hierarchically porous carbon with a template-free method. Sci. Rep. 4, 6349.
Gu, J., Wang, S., He, Z., Han, Y., Zhang, J., 2016. Direct synthesis of hydrogen peroxide from hydrogen and oxygen over activated-carbon-supported Pd–Ag alloy catalysts. Catal. Sci. Technol. 6, 809–817.
Gudarzi, D., Ratchananusorn, W., Turunen, I., Heinonen, M., Salmi, T., 2015. Promotional effects of Au in Pd–Au bimetallic catalysts supported on activated carbon cloth (ACC) for direct synthesis of H2O2 from H2 and O2. Catal. Today 248, 58–68.
Gudarzi, D., Ratchananusorn, W., Turunen, I., Heinonen, M., Salmi, T., 2015. Factors affecting catalytic destruction of H2O2 by hydrogenation and decomposition over Pd catalysts supported on activated carbon cloth (ACC). Catal. Today 248, 69–79.
Guo, N., Luo, W., Guo, R., Qiu, D., Zhao, Z., Wang, L., Jia, D., Guo, J., 2020. Interconnected and hierarchical porous carbon derived from soybean root for ultrahigh rate supercapacitors. J. Alloy. Compd. 834.
Han, G.H., Seo, M.G., Cho, Y.H., Han, S.S., Lee, K.Y., 2017. Highly dispersed Pd catalysts prepared by a sonochemical method for the direct synthesis of hydrogen peroxide. Mol. Catal. 429, 43–50.
Han, G.H., Lee, S.H., Hwang, S.Y., Lee, K.Y., 2021. Advanced development strategy of nano catalyst and DFT calculations for direct synthesis of hydrogen peroxide. Adv. Energy Mater. 11.
Hang, V.T.T., Chung, Y.M., 2020. Direct synthesis of H2O2 over Pd/C catalysts prepared by the incipient wetness impregnation method: Effect of heat treatment on catalytic activity. Korean J. Chem. Eng. 37, 65–71.
Henkelman, G., Uberuaga, B.P., Jónsson, H., 2000. A climbing image nudged elastic band method for finding saddle points and minimum energy paths. J. Chem. Phys. 113, 9901–9904.
Hu, B.Z., Deng, W.P., Li, R.S., Zhang, Q.H., Wang, Y., Delplanque-Janssens, F., Paul, D., Desmedt, F., Miquel, P., 2014. Carbon-supported palladium catalysts for the direct synthesis of hydrogen peroxide from hydrogen and oxygen. J. Catal. 319, 15–26.
Huang, Y., Liu, K., Kan, S., Liu, P., Hao, R., Liu, W., Wu, Y., Liu, H., Liu, M., Liu, K., 2021. Highly dispersed Fe-Nx active sites on Graphitic-N dominated porous carbon for synergetic catalysis of oxygen reduction reaction. Carbon 171, 1–9.
Huang, L., Wu, Q., Liu, S., Yu, S., Ragauskas, A.J., 2020. Solvent-free production of carbon materials with developed pore structure from biomass for high-performance supercapacitors. Ind. Crop. Prod. 150.
Humphrey, W., Dalke, A., Schulten, K., 1996. VMD: visual molecular dynamics. J. Mol. Graph. 14, 33–38.
Huynh, T.-T., Huang, W.-H., Tsai, M.-C., Nugraha, M., Haw, S.-C., Lee, J.-F., Su, W.-N., Hwang, B.J., 2021. Synergistic hybrid support comprising TiO2–carbon and ordered PdNi alloy for direct hydrogen peroxide synthesis. ACS Catal. 11, 8407–8416.
Ji, X., Chen, D.D., Peng, L., Frison, F., Dalla Valle, C., Tubaro, C., Zecca, M., Centomo, P., Ye, D.Q., Chen, P.R., 2021. Sustainable direct H2O2 synthesis over Pd catalyst supported on mesoporous carbon: the effect of surface nitrogen functionality. Catal. Today 376, 1–8.
Jia, W., Zhang, J., Le, F., Wang, X., Lv, Y., Cao, Y., Jia, D., 2020. Dual-nitrogen-source strategy for N-doped graphitic layer-wrapped metal carbide toward efficient oxygen reduction reaction. J. Colloid Interface Sci. 567, 165–170.
Kanungo, S., van Haandel, L., Hensen, E.J.M., Schouten, J.C., d'Angelo, M.F.N., 2019. Direct synthesis of H2O2 in AuPd coated micro channels: an in-situ X-Ray absorption spectroscopic study. J. Catal. 370, 200–209.
Kazici, H.C., Salman, F., Kivrak, H.D., 2017. Synthesis of Pd–Ni/C bimetallic materials and their application in non-enzymatic hydrogen peroxide detection. Mater. Sci.-Pol. 35, 660–666.
Kuhne, T.D., Iannuzzi, M., Del Ben, M., Rybkin, V.V., Seewald, P., Stein, F., Laino, T., Khaliullin, R.Z., Schutt, O., Schiffmann, F.,

Golze, D., Wilhelm, J., Chulkov, S., Bani-Hashemian, M.H., Weber, V., Borstnik, U., Taillefumier, M., Jakobovits, A.S., Lazzaro, A., Pabst, H., Muller, T., Schade, R., Guidon, M., Andermatt, S., Holmberg, N., Schenter, G.K., Hehn, A., Bussy, A., Belleflamme, F., Tabacchi, G., Gloss, A., Lass, M., Bethune, I., Mundy, C.J., Plessl, C., Watkins, M., VandeVondele, J., Krack, M., Hutter, J., 2020. CP2K: an electronic structure and molecular dynamics software package - quickstep: efficient and accurate electronic structure calculations. J. Chem. Phys. 152, 194103.

Lari, G.M., Puertolas, B., Shahrokhi, M., Lopez, N., Perez-Ramirez, J., 2017. Hybrid palladium nanoparticles for direct hydrogen peroxide synthesis: the key role of the ligand. Angew. Chem. Int. Ed. Engl. 56, 1775–1779.

Lee, S., Chung, Y.M., 2020. Direct synthesis of H2O2 over acid-treated Pd/C catalyst derived from a Pd-Co core-shell structure. Catal. Today 352, 270–278.

Lewis, R.J., Hutchings, G.J., 2018. Recent advances in the direct synthesis of H2O2. ChemCatChem 11, 298–308.

Li, T., Lin, H., Ouyang, X., Qiu, X., Wan, Z., 2019. In situ preparation of Ru@N-Doped carbon catalyst for the hydrogenolysis of lignin to produce aromatic monomers. ACS Catal. 9, 5828–5836.

Li, F., Shao, Q., Hu, M., Chen, Y., Huang, X., 2018. Hollow Pd–Sn nanocrystals for efficient direct H2O2 synthesis: the critical role of sn on structure evolution and catalytic performance. ACS Catal. 8, 3418–3423.

Liang, W.Y., Dong, J.F., Yao, M.Q., Fu, J.S., Chen, H.L., Zhang, X. M., 2020. Enhancing the selectivity of Pd/C catalysts for the direct synthesis of H2O2 by HNO3 pretreatment. New J. Chem. 44, 18579–18587.

B.G. Lippert, J.H. Parrinello, Michele, A hybrid Gaussian and plane wave density functional scheme, Molecular Physics, 92 (2010) 477-488

Lu, T., Chen, F., 2012. Multiwfn: a multifunctional wavefunction analyzer. J. Comput. Chem. 33, 580–592.

Lyu, J.H., Wei, J., Niu, L., Lu, C.S., Hu, Y.W., Xiang, Y.Z., Zhang, G.F., Zhang, Q.F., Ding, C.R., Li, X.N., 2019. Highly efficient hydrogen peroxide direct synthesis over a hierarchical TS-1 encapsulated subnano Pd/PdO hybrid. RSC Adv. 9, 13398–13402.

Maity, S., Eswaramoorthy, M., 2016. Ni–Pd bimetallic catalysts for the direct synthesis of H2O2– unusual enhancement of Pd activity in the presence of Ni. J. Mater. Chem. A 4, 3233–3237.

Mao, D., Jia, M., Qiu, J., Zhang, X.-F., Yao, J., 2019. N-doped porous carbon supported Au nanoparticles for benzyl alcohol oxidation. Catal. Lett. 150, 74–81.

Mao, J., Niu, D., Jiang, N., Jiang, G., Chen, M., Li, Y., Shi, J., 2020. Rational design of high nitrogen-doped and core–shell/mesoporous carbon nanospheres with high rate capability and cycling longevity for pseudocapacitive sodium storage. J. Mater. Chem. A 8, 9768–9775.

Momma, K., Izumi, F., 2011. VESTA 3for three-dimensional visualization of crystal, volumetric and morphology data. J. Appl. Cryst. 44, 1272–1276.

Nazeri, H., Najafi Chermahini, A., Mohammadbagheri, Z., Prato, M., 2021. Direct production of hydrogen peroxide over bimetallic CoPd catalysts: investigation of the effect of Co addition and calcination temperature. Green Energy Environ.

Nguyen, D.N., Sim, U., Kim, J.K., 2020. Biopolymer-inspired N-doped nanocarbon using carbonized polydopamine: a high-performance electrocatalyst for hydrogen-evolution reaction. Polymers (Basel) 12.

E. Ntainjua N, J.K. Edwards, A.F. Carley, J.A. Lopez-Sanchez, J.A. Moulijn, A.A. Herzing, C.J. Kiely, G.J. Hutchings, The role of the support in achieving high selectivity in the direct formation of hydrogen peroxide, Green Chemistry, 10 (2008).

Nugraha, M., Tsai, M.C., Rick, J., Su, W.N., Chou, H.L., Hwang, B. J., 2017. DFT study reveals geometric and electronic synergisms of palladium-mercury alloy catalyst used for hydrogen peroxide formation. Appl. Catal. a-Gen. 547, 69–74.

Oshima, C., Nagashima, A., 1997. Ultra-thin epitaxial films of graphite and hexagonal boron nitride on solid surfaces. J. Phys. Condens. Matter 9, 1–20.

Park, J., Nabae, Y., Hayakawa, T., Kakimoto, M.-A., 2014. Highly selective two-electron oxygen reduction catalyzed by mesoporous nitrogen-doped carbon. ACS Catal. 4, 3749–3754.

Perdew, J.P., Burke, K., Ernzerhof, M., 1996. Generalized gradient approximation made simple. Phys. Rev. Lett. 77, 3865–3868.

Piccinini, M., Edwards, J.K., Moulijn, J.A., Hutchings, G.J., 2012. Influence of reaction conditions on the direct synthesis of hydrogen peroxide over AuPd/carbon catalysts. Catal. Sci. Technol. 2, 1908–1913.

Priyadarshini, P., Ricciardulli, T., Adams, J.S., Yun, Y.S., Flaherty, D.W., 2021. Effects of bromide adsorption on the direct synthesis of H2O2 on Pd nanoparticles: formation rates, selectivities, and apparent barriers at steady-state. J. Catal. 399, 24–40.

Ricciardulli, T., Gorthy, S., Adams, J.S., Thompson, C., Karim, A.M., Neurock, M., Flaherty, D.W., 2021. Effect of Pd coordination and isolation on the catalytic reduction of O2 to H2O2 over PdAu bimetallic nanoparticles. J. Am. Chem. Soc. 143, 5445–5464.

Rio, S., Peru, G., Léger, B., Kerdi, F., Besson, M., Pinel, C., Monflier, E., Ponchel, A., 2020. Supported ruthenium nanoparticles on ordered mesoporous carbons using a cyclodextrin-assisted hard-template approach and their applications as hydrogenation catalysts. J. Catal. 383, 343–356.

K. Sheng, S. Zhang, J. Liu, S. E, C. Jin, Z. Xu, X. Zhang, Hydrothermal carbonization of cellulose and xylan into hydrochars and application on glucose isomerization, Journal of Cleaner Production, 237 (2019)

Shi, C., Hu, L., Guo, K., Li, H.Q., Zhai, T.Y., 2017. Highly porous carbon with graphene nanoplatelet microstructure derived from biomass waste for high-performance supercapacitors in universal electrolyte. Adv. Sustain. Syst. 1.

H.T. Thuy Vu, V.L. Nam Vo, Y.-M. Chung, Geometric, electronic, and synergistic effect in the sulfonated carbon-supported Pd catalysts for the direct synthesis of hydrogen peroxide, Applied Catalysis A: General, 607 (2020).

Tian, P., Ouyang, L., Xu, X., Xu, J., Han, Y.-F., 2013. Density functional theory study of direct synthesis of H2O2 from H2 and O2 on Pd(111), Pd(100), and Pd(110) surfaces. Chin. J. Catal. 34, 1002–1012.

Tian, P., Ouyang, L., Xu, X., Ao, C., Xu, X., Si, R., Shen, X., Lin, M., Xu, J., Han, Y.-F., 2017. The origin of palladium particle size effects in the direct synthesis of H2O2: is smaller better? J. Catal. 349, 30–40.

Tian, P., Xu, X., Ao, C., Ding, D., Li, W., Si, R., Tu, W., Xu, J., Han, Y.F., 2017. Direct and selective synthesis of hydrogen peroxide over palladium-tellurium catalysts at ambient pressure. ChemSusChem 10, 3342–3346.

Tian, P.F., Xuan, F.Z., Ding, D.D., Sun, Y., Xu, X.Y., Li, W., Si, R., Xu, J., Han, Y.F., 2020. Revealing the role of tellurium in palladium-tellurium catalysts for the direct synthesis of hydrogen peroxide. J. Catal. 385, 21–29.

VandeVondele, J., Hutter, J., 2007. Gaussian basis sets for accurate calculations on molecular systems in gas and condensed phases. J. Chem. Phys. 127, 114105.

Villa, A., Freakley, S.J., Schiavoni, M., Edwards, J.K., Hammond, C., Veith, G.M., Wang, W., Wang, D., Prati, L., Dimitratos, N., Hutchings, G.J., 2016. Depressing the hydrogenation and decomposition reaction in H2O2 synthesis by supporting AuPd on oxygen functionalized carbon nanofibers. Catal. Sci. Technol. 6, 694–697.

Vu, H.T.T., Vo, V.L.N., Chung, Y.M., 2021. Direct synthesis of hydrogen peroxide over palladium catalysts supported on glucose-derived amorphous carbons. Korean J. Chem. Eng. 38, 1139–1148.

Wang, V., Xu, N., Liu, J.-C., Tang, G., Geng, W.-T., 2021. VASPKIT: a user-friendly interface facilitating high-throughput computing and analysis using VASP code. Comput. Phys. Commun. 267.

Wei, H., Chen, J., Fu, N., Chen, H., Lin, H., Han, S., 2018. Biomass-derived nitrogen-doped porous carbon with superior capacitive performance and high CO2 capture capacity. Electrochim. Acta 266, 161–169.

Wilson, N.M., Priyadarshini, P., Kunz, S., Flaherty, D.W., 2018. Direct synthesis of H2O2 on Pd and AuxPd1 clusters: Understanding the effects of alloying Pd with Au. J. Catal. 357, 163–175.

Wilson, N.M., Schroder, J., Priyadarshini, P., Bregante, D.T., Kunz, S., Flaherty, D.W., 2018. Direct synthesis of H2O2 on PdZn nanoparticles: the impact of electronic modifications and heterogeneity of active sites. J. Catal. 368, 261–274.

Wu, Y.H., Gao, Z.X., Feng, Y.R., Cui, Q.N., Du, C.W., Yu, C.F., Liang, L., Zhao, W., Feng, J.L., Sun, J.H., Yang, R.Z., Sun, J.Y., 2021. Harnessing selective and durable electrosynthesis of H2O2 over dual-defective yolk-shell carbon nanosphere toward on-site pollutant degradation. Appl. Catal. B-Environ. 298.

Xu, Z.H., Zhang, X.M., Liang, Y., Lin, H.J., Zhang, S., Liu, J.L., Jin, C.D., Choe, U., Sheng, K.C., 2020. Green synthesis of nitrogen-doped porous carbon derived from rice straw for high-performance supercapacitor application. Energy Fuel 34, 8966–8976.

Yook, S., Kwon, H.C., Kim, Y.-G., Choi, W., Choi, M., 2016. Significant roles of carbon pore and surface structure in AuPd/C catalyst for achieving high chemoselectivity in direct hydrogen peroxide synthesis. ACS Sustain. Chem. Eng. 5, 1208–1216.

Zhang, R., Gu, X., Liu, Y., Hua, D., Shao, M., Gu, Z., Wu, J., Zheng, B., Zhang, W., Li, S., Huo, F., Huang, W., 2020. Hydrophilic nano-porous carbon derived from egg whites for highly efficient capacitive deionization. Appl. Surf. Sci. 512.

Zhang, M.J., Luo, Y.B., Wu, D.F., Li, Q., Xu, H.X., Cheng, D.J., 2021. Promoter role of tungsten in W-Pd/Al2O3 catalyst for direct synthesis of H2O2: modification of Pd/PdO ratio. Appl. Catal. a-Gen. 628.

Zhang, J., Shao, Q., Zhang, Y., Bai, S., Feng, Y., Huang, X., 2018. Promoting the direct H2 O2 generation catalysis by using hollow Pd-Sn intermetallic nanoparticles. Small 14, e1703990.

Zhu, J., He, C., Li, Y., Kang, S., Shen, P.K., 2013. One-step synthesis of boron and nitrogen-dual-self-doped graphene sheets as non-metal catalysts for oxygen reduction reaction. J. Mater. Chem. A 1.